Mapping the global variation in the efficiency of ocean alkalinity enhancement for carbon dioxide removal

Mengyang Zhou

mengyang.zhou2024@gmail.com

University of Connecticut https://orcid.org/0000-0002-2155-506X

Michael Tyka

Google

David Ho

University of Hawai□i at Mānoa; [C]Worthy

Elizabeth Yankovsky

[C]Worthy

Scott Bachman

[C]Worthy; National Center for Atmospheric Research

Thomas Nicholas

[C]Worthy

Alicia Karspeck

[C]Worthy

Matthew Long

[C]Worthy; National Center for Atmospheric Research

Article

Keywords:

Posted Date: March 19th, 2024

DOI: https://doi.org/10.21203/rs.3.rs-4124909/v1

Additional Declarations: There is **NO** Competing Interest.

Version of Record: A version of this preprint was published at Nature Climate Change on November 8th, 2024. See the published version at https://doi.org/10.1038/s41558-024-02179-9.

Mapping the global variation in the efficiency of ocean alkalinity enhancement for carbon dioxide removal

Mengyang Zhou[1,*], Michael D. Tyka[2,*], David T. Ho[3,4], Elizabeth Yankovsky[4], Scott Bachman[4,5], Thomas Nicholas[4], Alicia R. Karspeck[4], Matthew C. Long[4,5]

[1]Department of Marine Sciences, University of Connecticut, Groton, CT, USA

[2]Google Inc., 601 N 34th St, Seattle, WA 98103, USA

[3]Department of Oceanography, University of Hawai'i at Mānoa, Honolulu, HI, USA

[4][C]Worthy, LLC, Boulder, CO, USA

[5]National Center for Atmospheric Research, Boulder, CO, USA

*These authors contributed equally to this work.

Correspondence: Mengyang Zhou (mengyang.zhou2024@gmail.com), Michael D. Tyka (mike.tyka@gmail.com)

Abstract

To limit global warming to below 2°C by 2100, carbon dioxide removal (CDR) from the atmosphere will be necessary. Ocean alkalinity enhancement (OAE) is a promising approach to achieving CDR at scale. However, OAE deployments are subject to incomplete air-sea CO_2 equilibration — reducing the efficiency of carbon removal. Here, we generated the first global maps of OAE efficiency, including an assessment of the seasonal variation in efficiency. We show that the equilibration kinetics exhibit two characteristic timescales — rapid surface equilibration followed by a slower second phase, representing the re-emergence of excess alkalinity that was initially subducted. These kinetics vary considerably with latitude and the season of alkalinity release, both critical considerations for the placement of prospective OAE deployments. We also calculated histograms quantifying the spatial and temporal scales of the induced CO_2 uptake and thus identifying the requirements for modeling OAE in regional ocean models.

Main

Limiting climate warming to below 1.5°C or 2°C requires — in addition to rapid reductions in greenhouse gas emissions — removing hundreds of billions of tons of CO_2 from the atmosphere by the end of the century[1,2]. Marine carbon dioxide removal (mCDR) technologies have gained recent attention due to their potential to reach climate-relevant scales. However, quantifying the net carbon removal attained by mCDR technologies is challenging because the ocean is highly dynamic; signals associated with mCDR interventions are advected away from source regions and easily lost in the noise of background variability[3]. Notably, the efficiency of mCDR deployments is expected to vary geographically and with seasonal and interannual variability in ocean conditions and circulation patterns. Such variations are important to consider when developing quantitative assessments of the net carbon removal achieved by mCDR deployments.

Ocean alkalinity enhancement (OAE) is a promising approach to mCDR[4]. OAE aims to accelerate natural rock weathering processes that regulate atmospheric CO_2 on millennial timescales[5,6]. Increasing alkalinity in the ocean drives the seawater carbon system equilibrium chemistry toward bicarbonate (HCO_3^-) and carbonate (CO_3^{2-}) ions[7,8], causing a pCO_2 decrease that, at the surface, can stimulate a net transfer of CO_2 from the atmosphere. However, equilibration of CO_2 across the air-sea interface is relatively slow due to the buffering effect of carbonate chemistry[9], raising the possibility that circulation and mixing can remove excess alkalinity from the surface ocean before the full potential for CO_2 transfer is achieved[10]. Therefore, the efficiency of OAE deployments is contingent on geographic patterns in ocean circulation as well as variations in surface ocean carbonate chemistry and wind speed that determine gas exchange kinetics. We define the evolution of OAE efficiency with time $\eta(t)$ as:

$$\eta(t) = \frac{\Delta DIC(t)}{\Delta Alk} \quad (1)$$

where ΔAlk is the total amount of excess alkalinity added to the surface ocean over a discrete time interval, and $\Delta DIC(t)$ represents the increase of ocean dissolved inorganic carbon (DIC) inventory through time owing to the alkalinity addition. The local maximum OAE efficiency that can be achieved once re-equilibration is fully established by air-sea CO_2 exchange depends on

the temperature and background carbonate system and varies over the global ocean between about 0.7 and 0.9[8,11,12] (Supplementary Fig. 1).

Regional and global coupled physical-biogeochemical ocean models, as well as Earth system models, have been used to simulate alkalinity addition[13–17] and estimate OAE efficiency[3,10,11,18]. These studies revealed spatio-temporal variations of OAE efficiency, yet they were done either at the basin scale, the full global scale or in limited/sparse patches and timings.

Here, we present the first global, multi-season maps of OAE efficiency simulated using a global circulation model, based on 690 individual alkalinity pulse locations and four seasons. This study aims to determine regions in the ocean and seasons that are most effective for OAE deployments. Further, while early OAE deployments are most likely to occur in near-coastal regions due to proximity to infrastructure, energy supply, and human resources, the global coverage of our study comprehensively illustrates the controls on OAE efficiency, thereby enabling understanding and mechanistic insight that is important to advance frameworks for quantitative assessments of OAE-mediated net carbon removal. The numerical experiments we conducted comprise a collection of Impulse-Response Function (IRF) curves, which characterize the response of CO_2 uptake to OAE. We explore the patterns in our data by fitting the kinetics of CO_2 uptake with a conceptual 3-box model and characterize the spatial and temporal variations of CO_2 uptake at different release locations.

Spatial and seasonal variations of OAE efficiency

The pulsed addition of excess alkalinity to the surface ocean induces uptake of CO_2 from the atmosphere, increasing the total DIC inventory relative to an unperturbed reference simulation. The time evolution of the efficiency factor $\eta(t)$ varies considerably by injection location and season (Fig. 1; Supplementary Fig. 2). Generally, η is higher when the alkalinity is added in summer versus winter (Fig. 1; Supplementary Fig. 2). The spatial patterns in OAE efficiency and its seasonal variation are most pronounced at short time-horizons (e.g., Fig. 1a, e), with the highest short-term efficiency evident at subpolar latitudes. As the simulations continue, however, both the spatial and seasonal variability are reduced (Fig. 1c, g). For example, efficiency in the tropics is largely comparable to that at subpolar latitudes after 15

years of simulation (Fig 1c, g). Persistent low efficiency is evident at polar latitudes, such as in the Labrador and Norwegian Seas as well as the Weddell and Ross Seas in the Southern Ocean. After 15 years, the efficiency in these regions increases minimally, consistent with deep winter mixing essentially irreversibly removing alkalinity from the surface ocean (Fig. 1c, g). Finally, the subtropical gyre regions show relatively low efficiency on short time scales and, while the efficiency in these regions continue to increase over the 15-year simulations (Fig. 1), it remains lower than the efficiency simulated in the tropics and subpolar latitudes.

Representative locations

Release locations with representative CO_2 uptake curves and re-equilibration timescales are presented in Figure 2. When adding alkalinity in January in the Labrador Sea, a large fraction of the added alkalinity is quickly subducted to depths below 1000 m, where it remains out of contact with the atmosphere — likely for timescales of 100s of years (Fig. 2a)[19]. The resultant $\eta(15)$ is 0.2 if alkalinity is added in January, but 0.7 in July, when surface ocean stratification allows a great proportion of the alkalinity to remain in the surface layer.

The Gulf of St. Lawrence is among the best locations for OAE deployment in terms of rapid CO_2 re-equilibration (Fig. 2b); other shallow semi-enclosed seas such as the North Sea have similar dynamics. The stratification in this region keeps the added alkalinity near the surface and the initial CO_2 gas exchange is fast (Fig. 2b). As a result, η arrives at the maximum value of 0.8 after only 2 years following alkalinity addition (Fig. 2b). This location also exhibits minimal seasonal variations in η.

The simulations in the North Atlantic subtropical gyre show CO_2 uptake curves gradually rising with time (Fig. 2c). The added alkalinity is subducted to depths with a subsurface maximum between 100 and 500 m. A slow but steady increase in CO_2 uptake is ongoing and will continue beyond the 15 years of model integration, mediated by re-emergence of the excess alkalinity, brought back to the surface from depth by shallow overturning circulation and deep winter mixing (Fig. 2c).

Finally, adding alkalinity in the equatorial Atlantic Ocean resulted in CO_2 uptake at a steady pace (Fig. 2d) and η evolved with minimum seasonality, reaching a maximum of 0.8 after year 10.

CO_2 equilibration dynamics in the Lagrangian frame

We developed a simple, conceptual box model (shown in Fig. 3, see Supplementary for full derivation) to provide a heuristic framework explaining the variety of equilibration dynamics seen in the simulations (Fig. 1, 2). The model aims to describe CO_2 equilibration in the Lagrangian frame of the alkalinity plume using a small number of meaningful parameters. Early in the plume's spreading trajectory, the air-sea CO_2 equilibration proceeds with an e-folding timescale τ_a. Gradually, however, over a timescale of $\sim\tau_\ell$, the equilibration slows down as alkalinity is removed from the surface layer; CO_2 uptake then proceeds with an e-folding timescale τ_b. The final parameter, η_{max}, determines the ultimate $\Delta[DIC]/\Delta[Alk]$ at complete equilibration; η_{max} varies between 0.79 and 0.9. Overall, this two-stage scheme is capable of closely fitting the equilibration curves and the geographic structure evident in their variability. All four parameters vary primarily with latitude, approximately symmetrically in the northern and southern hemispheres (Fig. 4; Supplementary Fig. 1), with comparably little zonal variation. Supplementary Figure 3 shows the fits for various individual locations.

In addition to fitting the conceptual model directly to the efficiency curves, we also independently compute the temporal evolution of metrics that are similar to the parameters using diagnostic fields output by the model. The curve-fitting provides a concise summary of the uptake dynamics, while an examination of these explicit metrics provides confirmatory mechanistic insight. The air-sea equilibration timescale is computed as $\tau = \beta z_{ml}/k$, where $\beta = \partial[DIC]/\partial[CO_2]$ (i.e., the ionization fraction), z_{ml} is the mixed layer depth that is quantified as z_0/μ where z_0 is the thickness of the top layer (10 m) and μ is the fraction of alkalinity in the surface layer, and k is the gas transfer velocity. The results are presented in Figure 5 for the four representative locations shown in Figure 2.

The deep water formation regions in the North Atlantic and Southern Oceans are characterized by a τ_ℓ considerably shorter than τ_a and an extremely long τ_b (Fig. 4a). For example, alkalinity addition in January in the Labrador Sea resulted in τ_a, τ_ℓ, and τ_b of 90, 10, and 1708 months, respectively (Supplementary Fig. 3a). This result is consistent with the rapid decline of the fraction of added alkalinity remaining in the surface layer (Fig. 5a-ii), after which the CO_2 deficit is almost entirely prevented from equilibration. The strong separation of

timescales τ_a and τ_b results in an uptake curve with a sharp appearance of a plateau and little further progress past $\sim\tau_\ell$ years. τ_a is strongly seasonal owing to seasonal variations in convectively-driven mixing and subduction of alkalinity, which determines the total amount of equilibration that can occur before contact with the atmosphere is lost. While the alkalinity is at the surface, however, the equilibration in the Labrador Sea is relatively fast, owing to the low β factor and high k (Fig. 5a).

In the subpolar oceans at ~50°S and ~50°N, a pronounced minimum appears in τ_a while τ_ℓ remains large relative to the high latitudes or subtropics (Fig. 4). Together this forms a band of rapid equilibration that is not interrupted by transition to a second slower phase. These areas, especially the Southern Ocean and the North Pacific, exhibit ideal areas for OAE deployment from the standpoint of rapid equilibration. For example, the simulation in January in the Gulf of St. Lawrence is characterized by τ_a, τ_ℓ and τ_b of 7, 29, and 22 months, respectively (Supplementary Fig. 3c). The behavior of k and β remain similar, but the surface residence time of excess alkalinity is vastly prolonged. The steady increase in the gas exchange time scale is largely driven by the surface dilution of excess alkalinity (Fig. 5b).

In the subtropical latitudes, the situation is once again reversed with τ_a rising and τ_ℓ reaching a minimum around 30°N and 30°S (Fig. 4). This is consistent with two distinct equilibration phases: alkalinity is removed from the surface relatively rapidly owing to convergent surface flow and subduction to intermediate depths. However, this lost excess alkalinity is subsequently re-exposed in the shallow subtropical overturning circulation. The example in the North Atlantic Subtropical Gyre in January shows τ_a, τ_ℓ, and τ_b of 36, 21, and 143 months, respectively (Supplementary Fig. 3e). Unlike the deep water formation areas, τ_b is still small enough to permit eventual equilibration on the timescale that we project to be about 20 - 50 years (Fig. 4). Due to this re-emergence of the subducted alkalinity, these regions deviate most strongly from a simple single-exponential model—which would describe equilibration only by surface CO_2 exchange and a surface residence e-folding time[9]. The sluggish initial equilibration is due to lower k and high β. Notably, however, while the alkalinity is subducted, it remains in the thermocline, allowing the subsequent re-emergence and continued

uptake (Fig 2c-iii). These areas also exhibit very strong seasonality owing to changes in τ_a that is driven by seasonal changes in mixed layer depth (Fig. 4a).

In general, τ_a is much smaller than τ_b, but the two timescales converge and become almost equal at the equator (Fig. 4d). Thus, the equilibration at the equator is essentially characterized by a single exponential curve with a more or less constant τ. Comparatively, however, the overall e-folding time associated with air-sea CO_2 equilibration is relatively slow in the equatorial region, requiring on the order of 10 - 20 years (Fig. 4a). The relatively constant τ is the confluence of two compensating factors. The total amount of excess alkalinity at the surface continues to decline through subduction, which on its own should slow the equilibration timescale; however, it is compensated by an increase in the average k and a significant decline in β (Fig. 5d). Together these effects cancel, resulting in a more or less constant τ (Fig. 5d). None of the parameters exhibit any seasonality at the equator.

Spatial extents of CO_2 uptake

Simulations with a global model can account for all air-sea CO_2 exchange after OAE deployments, presuming the model is integrated for long enough. However, there is substantial interest in simulating OAE in regional models, which can represent circulation with much higher fidelity over finite domains, but cannot account for OAE-induced CO_2 uptake outside the domain boundaries. Estimates of the spatial distribution of CO_2 uptake can help determine the domain size needed to capture the majority of CO_2 uptake for different regions. The percentage of total CO_2 uptake in 15 years that can be enclosed at a certain distance from the injection center is presented in Figure 6a-c, for radii of 500 km, 1000 km and 2000 km respectively. The spatial patterns are similar at different cutoffs, with the most locally constrained uptake occurring nearest to the poles and in the subpolar regions where 70-90% occurs within 1000 km. The most geographically spread-out uptake occurs in the tropics and in the western boundary currents, where less than 60% of equilibration occurs even within 2000 km, owing to the rapid horizontal transport.

For example, in the Labrador Sea, 34% of the total CO_2 uptake in 15 years occurred during the first 3 months following alkalinity addition, but this fraction decreased dramatically in later months when the system quickly transitioned from the early to late stage (Fig. 6d). Overall, 79%

of the total CO_2 uptake in 15 years occurred within 1000 km (and 98% within 2000 km) of the injection center (Fig. 6d). In the Gulf of St. Lawrence, the majority (93%) of the total CO_2 uptake in 15 years occurred in the first 2 years (Fig. 6e-i). The uptake was also confined locally, with 92% occurring within 1000 km of the injection site (Fig. 6e-i), making this location ideal for modeling OAE with regional ocean models. CO_2 uptake was much more spread out in space and time for OAE deployments in the subtropical gyre and equatorial ocean, where η gradually increases as shown in Figure 2 (Fig. 6f, g). In the example of the subtropical gyre, 62% of the total uptake occurred within 1000 km (and 78% within 2000 km) of the injection site. In the equatorial example, only 44% of the total uptake occurred within 1000 km (and 66% within 2000 km) of the injection site.

Discussion

Here, we present the first global, multi-seasonal map of OAE efficiency with regional specificity. Our findings show that in many places, the efficiency of OAE depends not only on the gas transfer velocity[20,21], but is also sensitive to the subduction and re-emergence dynamics mediating the amount of alkalinity retained in the surface layer. Crucially, a significant fraction of the CO_2 equilibration occurs many years after and far away from the initial alkalinity modification event. We developed a heuristic model capable of summarizing uptake dynamics with a few parameters: rapid and slow exchange timescales, a timescale characterizing the transition between these two regimes, and the ultimate uptake efficiency. In general, alkalinity deployed at subpolar latitudes induces rapid CO_2 uptake due to fast gas exchange. The spatial variability and the differences in efficiency across seasons diminishes with time following deployment. While our integrations were only 15 years in length, we anticipate that nearly all of the subpolar and low-latitude ocean can achieve the thermodynamically-feasible maximum uptake from OAE within one to two decades, with a possible exception of the subtropical gyres, which have slightly diminished efficiency. High latitude regions, by contrast, are subject to deep mixing and removal of alkalinity from the surface layer that is essentially irreversible on decadal timescales. In addition to these broad patterns, we identified regions characterized by fast, local CO_2 re-equilibration and low seasonality. Regions with such dynamics may be optimal locations for the first experimental OAE deployments.

Our study has the following limitations. Our model integrations sampled only a single deployment year, thus we have not characterized the effect of interannual climate variability (IAV) on uptake dynamics. We anticipate that the importance of IAV varies regionally and this is currently being investigated (Yankovsky et al., *in prep*). Further, while our analysis has provided robust mechanistic insight, we expect the specific details of simulated uptake efficiency and its seasonal and geographic variation to be somewhat model-dependent. Future studies should compare results across multiple models and consider specifically the effect of representations of vertical mixing, spatial resolution, and particular phenomenology, such as filamentation and submesoscale dynamics. Finally, MARBL (the Marine Biogeochemistry Library)[22] was configured in this study to preclude feedback of alkalinity on biogenic calcification rates; if the magnitude of alkalinity perturbations is large, this feedback—and perhaps other alkalinity cycling mechanisms—may exert important control on the ultimate efficiency[23].

Despite these caveats, this study provides an important characterization of geographic and seasonal variations in OAE efficiency, which, coupled with data characterizing techno-economic constraints, can be used to provide broad guidance in evaluating the viability of OAE deployment. A well-functioning carbon removal market requires robust methods to quantify net carbon removal achieved by interventions. Our results demonstrate the large spatiotemporal scales involved, indicating that numerical models must play a critical role in verification approaches. Further, the experiments we conducted generated a collection of regionally-specific IRFs curves. Maps of this nature may have an important role to play in future systems supporting the characterization of net carbon removal for market quality Monitoring, Reporting and Verification (MRV).

Methods

Experimental design and global OAE forcing pattern

We simulated one-month-long pulse injections of alkalinity to the surface ocean in a global forced ocean-ice (FOSI) configuration of the Community Earth System Model version 2 (CESM2)[24]. The FOSI configuration is detailed in Yeager et al. (2022)[25]. Briefly, the ocean component was the Parallel Ocean Program version 2 (POP2), integrated at a nominal

horizontal resolution of 1° x 1°. POP2 was coupled to the Marine Biogeochemistry Library (MARBL)[22]. The model was forced with the Japanese 55-year atmospheric reanalysis dataset (JRA55)[26] and was integrated from 1850 to near-present, repeating the 1958-2018 period of the JRA55 forcing and including the historical transient in atmospheric CO_2 — thus the simulated ocean DIC fields include an anthropogenic component.

All simulations in this study were forced with historical atmospheric CO_2. It is important to note that the simulated efficiency of OAE depends on assumptions related to the time evolution of atmospheric CO_2 [27]. Here, we assume that each alkalinity perturbation is sufficiently small to generate a negligible impact on atmospheric CO_2. Controls on the atmospheric CO_2 growth rate are dominated by other factors in the Earth system, including emissions and large-scale terrestrial and ocean carbon sinks[28].

For the simulations in this study, we use the two carbonate systems simulated in parallel online within MARBL[22]. Computing the effect of mCDR requires establishing a baseline counterfactual condition — i.e., the temporal evolution of air-sea CO_2 gas exchange in the absence of the mCDR intervention. The two carbonate systems in MARBL enable simulating both the factual and counterfactual conditions in a single integration of the model. The POP2 and MARBL code was modified to permit applying an alkalinity surface forcing term to the primary MARBL carbonate system alkalinity tracer; the atmospheric CO_2 boundary condition was set to be identical for both systems, and the DIC and alkalinity tracers for both systems were initialized to identical values. Since the DIC and alkalinity tracers for the two carbonate systems share the same atmospheric CO_2 forcing, ocean transport, and biologically-mediated source/sink terms, the unperturbed carbonate system provides a representation of the baseline counterfactual and the difference between the simulated tracers and fluxes from the perturbed and unperturbed carbonate systems enables computing net CO_2 removal — termed "additionality" — as well as the anomaly induced in alkalinity, DIC, and pCO_2 distributions. Note that the validity of this approach is contingent on the assumption that feedback between carbonate chemistry and the biologically-mediated source/sink terms is negligible; this assumption is satisfied in this configuration of MARBL.

To reveal the spatial variations of OAE efficiency, the global ocean was divided into a total of 690 patches up to 75°N, with 310 patches located in the Exclusive Economic Zone (EEZ, 370 km from the coastline) and 380 in the open ocean (Supplementary Fig. 4). The EEZ was separated from the open ocean, allowing for a higher resolution in the coastal oceans. An unsupervised machine learning algorithm, K-means clustering, was trained separately on the EEZ and open ocean grid points (based on their longitudes and latitudes) to generate unstructured OAE forcing patches with approximately similar surface areas. The resulting patch areas varied within ±80% of the median value (2.4×10^5 km^2) in the EEZ and ±86% of the median values (7.2×10^5 km^2) in the open ocean (Supplementary Fig. 5). Patches in the high latitudes ended up with smaller areas due to the Earth's curvature. Note that while the goal of this clustering approach was to create patches with approximately similar areas, allowing for the irregularity of coastlines, the study results are not intimately dependent on having identical areas as the same area-normalized alkalinity flux was applied to each region. Further, the study design was extended incrementally as additional computing resources became available. We initially anticipated being able to complete integrations only for the North Atlantic and North Pacific, hence our patch region mask was constructed to cover only these basins with some extension into the southern hemisphere. As additional computing resources became available, we completed integrations for the southern hemisphere, excluding the Antarctic zone south of 60°S — we then subsequently decided to conduct additional experiments in the Antarctic zone. This incremental addition of regions resulted in linear alignment of region boundaries south of the Equator and at 60°S (Supplementary Fig. 4). These aligned boundaries create the impression of sharp divisions in some of the mapped results, but this is a visual artifact that should not be interpreted as a meaningful geophysical feature.

Alkalinity was added to each patch at the ocean surface for one month at a constant rate of 10 mol m^{-2} yr^{-1}. He and Tyka (2023)[10] found that it was possible to sustain a flux of this magnitude in most of the coastal ocean while maintaining the change in pH to be < 0.1 and the change in aragonite saturation state (Ω_{arag}) to be < 0.5. The maximum change of pH and Ω_{arag} in the ocean from our simulations was 0.085 and 0.42, respectively (Supplementary Fig. 6). To reveal the seasonal variations of OAE efficiency, four individual simulations were done for each

patch with alkalinity added in January, April, July, and October 1999. After the alkalinity addition, each simulation was run for 15 years. Note that this study does not assess how interannual variability might modulate OAE efficiency. This is an important subject to examine but is left to future work (Yankovsky et al., *in prep*). Further, all the experiments sample a particular period (i.e., 1999-2014) during the ongoing transient rise of atmospheric CO_2.

A parametric model for CO_2 equilibration dynamics in the Lagrangian frame

A parametric model was developed, based on the commonly used mixed-layer gas-exchange model[7], in which an initially induced DIC deficit $\Delta[DIC](0)$ will be replenished by air-sea CO_2 exchange according to a single exponential function of the form

$$\Delta[DIC](t) = \Delta[DIC](0)e^{-\frac{t}{\tau}} \quad (2)$$

where the e-folding time is $\tau = \beta z_{ml}/k$. This e-folding time τ is determined by the gas transfer velocity, k (parameterized as a function of wind speed squared[20,21]), the depth of the exchanging ocean reservoir, z_{ml}, and the factor $\beta = \partial[DIC]/\partial[CO_2]$, which accounts for the fact that the effective capacity of the ocean for CO_2 is vastly increased due to the fast carbonate equilibrium with HCO_3^- and CO_3^{2-} ions. The factor β depends on the local carbonate system state and varies over the global ocean; a typical value is around 10-20.

This simple model assumes that all the exchange parameters in the expression for τ remain constant. However, most of the equilibration curves obtained from our simulations (Fig. 2; Supplementary Fig. 3) do not fit such a single exponential form, which indicates that the CO_2 equilibration of an alkalinized plume in its Lagrangian frame cannot be modeled by a constant e-folding time. Instead, the average surface parameters of gas exchange (k and β) change as the plume spreads and mixes with adjacent water masses. Further, the ocean circulation and mixing result in a removal of alkalinity from the surface ocean, resulting in an increase in the depth of the plume over time.

Thus, we expanded the simple gas-exchange model to allow for gradual changes in the gas exchange parameters by introducing two different plume states “a” and “b”, where all of the $\Delta[DIC](0)$ deficit starts in state “a” and gradually transitions to state “b”, on a timescale set by an additional parameter, τ_ℓ (Fig. 3).

The early plume state "a" represents the period when the excess alkalinity is still near the surface, it has not been transported far from the source region, and gas exchange is mediated by a local gas transfer velocity, k_a, and CO_2 sensitivity, $\beta_a = \partial[DIC]_a/\partial[CO_2]_a$. Since gas exchange occurs only from the top-most simulation layer (of thickness z_0 = 10 m), which contacts the atmosphere, the exchange rate is proportional to the fraction of alkalinity retained in this top layer, which we call the surface dilution factor μ. Together, these parameters directly determine the resultant gas exchange e-folding time τ_a.

$$\tau_a = \frac{z_0}{\mu_a} * \frac{\beta_a}{k_a} \tag{3}$$

The quantity z_0/μ_a can be understood as a metric quantifying the effective mixing depth. Over time, the excess alkalinity is mixed away from the surface. It is advected horizontally in regional circulation, resulting in a late plume state characterized by the parameters μ_b, β_b, and k_b, and therefore

$$\tau_b = \frac{z_0}{\mu_b} * \frac{\beta_b}{k_b} \tag{4}$$

Our model transitions between these two states exponentially: the fraction of the starting deficit in state "a" is $a(t) = exp\ (-t/\tau_\ell)$, while the remainder is in state "b" (See Fig. 3).

This model predicts the uptake curve to take the following form (See Supplementary for a rigorous derivation):

$$\frac{\eta(t)}{\eta_{max}} = 1 - Qe^{-\frac{t}{\tau_{a\ell}}} - (1-Q)e^{-\frac{t}{\tau_b}} \tag{5}$$

where

$$\tau_{a\ell} = \frac{1}{\frac{1}{\tau_a} + \frac{1}{\tau_\ell}} = \frac{\tau_a \tau_\ell}{\tau_a + \tau_\ell} \tag{6}$$

and

$$Q = \frac{\tau_a \tau_\ell - \tau_b \tau_\ell}{\tau_a \tau_\ell - \tau_b \tau_\ell - \tau_a \tau_b} \tag{7}$$

This equilibration curve is parameterized by four free parameters. The characteristic timescales τ_a and τ_b represent the surface gas exchange in the early and late plumes, respectively. The timescale τ_ℓ represents the speed at which the plume transitions from state "a" to state "b". Finally, η_{max} is the overall scaling parameter, which is the equivalent of $\Delta[DIC]/\Delta[Alk]$ of the

carbonate system (typically in the range of 0.79-0.90) and sets the maximum amount of CO_2 absorbed by one mol of alkalinity.

Further, this model predicts the surface dilution $\mu(t)$ to follow an exponential interpolation of the form:

$$\mu(t) = \mu_a e^{-\frac{t}{\tau_\ell}} + \mu_b \left(1 - e^{-\frac{t}{\tau_\ell}}\right) \quad (8)$$

which is determined by three parameters: μ_a and μ_b set the surface dilution in the early and late plume stages and τ_ℓ, again, represents the speed at which the plume states transition.

For each release location/season (2760 in total), we simultaneously fit the above model to the surface dilution and equilibration curve, where τ_ℓ was shared between the two curves. To obtain fits, each parameter was set to an initial set of starting values (τ_a = 10 months, τ_ℓ = 15 months, τ_b = 25 months, μ_a = 0.2, μ_b = 0.05). The parameter η_{max} was initialized to a value obtained by calculating $\Delta[DIC]/\Delta[Alk]$ from the carbonate model, smoothed with a gaussian kernel (σ=20°) across latitudes. The combined squared error between the analytic curves and the curves obtained from the simulation was calculated and all six parameters were minimized using gradient descent until they stabilized. The parameter η_{max} was constrained to vary ±0.01 from its starting value. Further details of the fitting procedure are found in the Supplementary.

Calculations of τ and its components in the Lagrangian scheme

To understand what drives air-sea CO_2 equilibration timescale (τ) in the Lagrangian frame of alkalinity plumes, we calculated individual contributions of β, k, and z_{ml} to τ and their changes over time directly from the simulation output. To account for the spread of alkalinity plumes through time, we calculated properties averaged over the plumes. Specifically, β and k were weighted by surface air-sea CO_2 flux at each time, so regions with stronger CO_2 uptake play a more important role in setting the overall property values. We also calculated the fraction of added alkalinity remaining in the surface layer (top 10 m) as the effective mixed layer depth, z_{ml}. The value of τ at each time step can therefore be calculated using $\tau = \beta z_{ml}/k$.

Assessing the spread of CO_2 uptake

We evaluated how the CO_2 uptake was distributed in both space and time following each addition of alkalinity. We first calculated the percentage of the total CO_2 uptake in 15 years that occurred at each grid point and each time step. For each injection simulation, we calculated the percentage of the total CO_2 uptake in 15 years that occurred at each grid point and each time step. We then computed cumulative histograms over the spatial and temporal distributions of this uptake, capturing where and when uptake occurs for alkalinity addition at each location, respectively.

Data availability

The data of the CESM2 simulation output (i.e. the primary dataset in this study) are being archived in analysis-ready cloud-optimized format (cite https://ieeexplore.ieee.org/abstract/document/9354557) in an open access AWS bucket kindly provided by Source Cooperative, and can be found at https://beta.source.coop/repositories/cworthy/oae-efficiency-atlas/. The CESM2 netCDF output files are provided, as well as a sidecar file of kerchunk references, which together allow the entire dataset to be accessed via the Zarr protocol. This facilitates interpretation and extension of the research in this article, via parallel analysis of the entire dataset (∼200TB of data when uncompressed) by accessing it as a single Xarray dataset (cite https://openresearchsoftware.metajnl.com/articles/10.5334/jors.148). Instructions for doing so can be found in the README.md file included with the data.

Code availability

The code for simulating OAE in CESM2 and data analysis are available on GitHub: https://github.com/CWorthy-ocean/oae-dor-global-efficiency

Acknowledgments

This material is based on work supported by the National Center for Atmospheric Research, a major facility sponsored by the National Science Foundation under Cooperative Agreement No. 1755088. Any opinions, findings, conclusions, or recommendations expressed in this material do not necessarily reflect the views of the National Science Foundation.

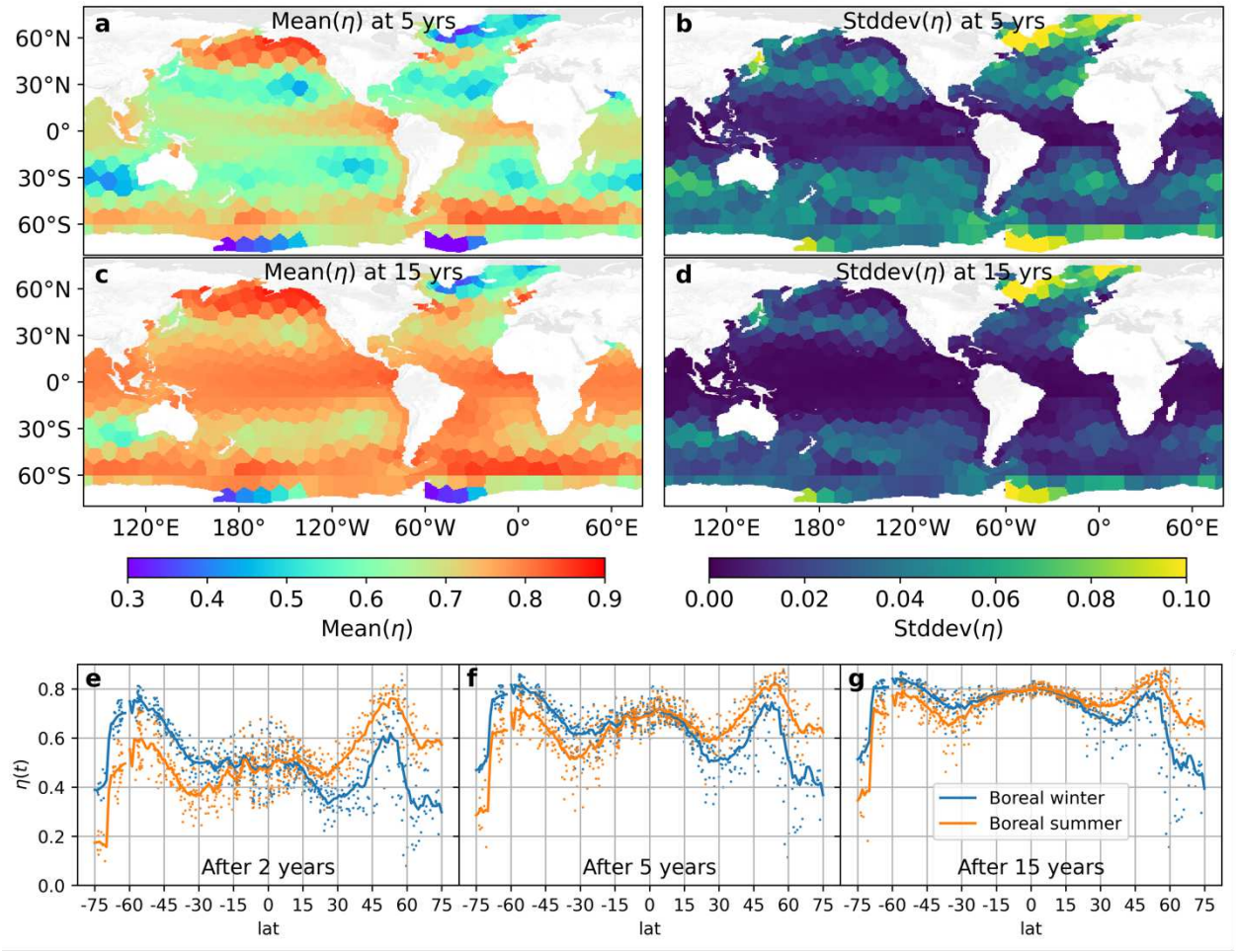

Figure 1. Seasonal mean of OAE efficiency (η) after 5 years (a) and 15 years (c) for one-month alkalinity pulses added in each patch. Panels (b) and (d) show the respective standard deviation between releases done in January, April, July, and October at the 5 and 15 year mark, respectively. Panels (e), (f), and (g): Plots of $\eta(2)$, $\eta(5)$, and $\eta(15)$ against latitude for January and July releases.

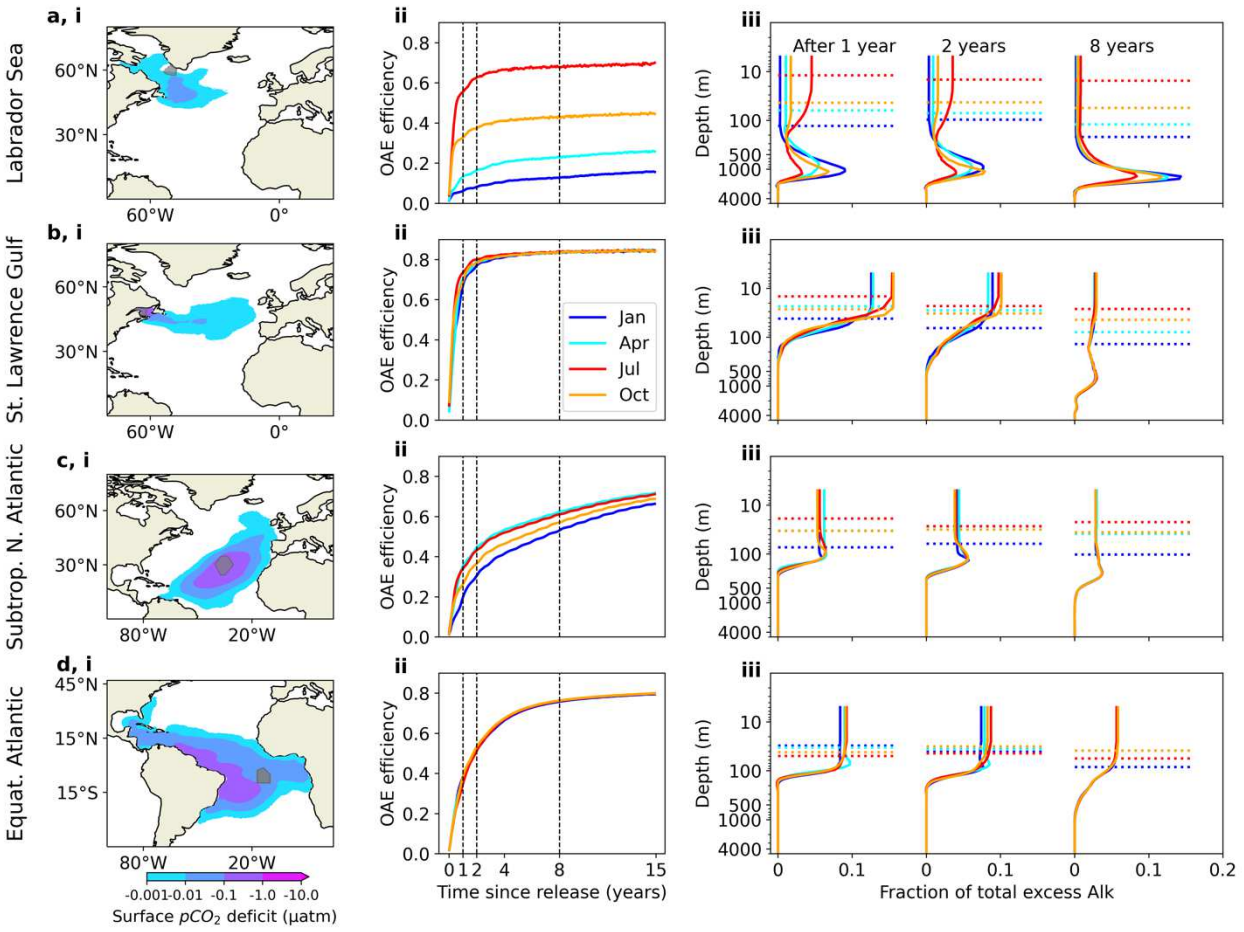

426

427 Figure 2. Pulse additions of alkalinity to four representative locations in the (a) Labrador Sea, (b)
428 Gulf of St. Lawrence, (c) subtropical North Atlantic, and (d) equatorial Atlantic. (i) Surface pCO_2
429 deficit after 2 years following alkalinity additions in January. Animations of the evolution of
430 surface pCO_2 deficit are attached in the supplements. Release locations are shown in gray
431 patches. (ii) The increase of DIC inventory, normalized by the amount of alkalinity added, over
432 the 15 years following alkalinity additions in 4 seasons. (iii) Vertical distribution of the fraction
433 of the added alkalinity after 1, 2, and 8 years following alkalinity additions, with the dotted
434 horizontal line denoting mixed layer depth weighted by surface CO_2 flux at the corresponding
435 time point.

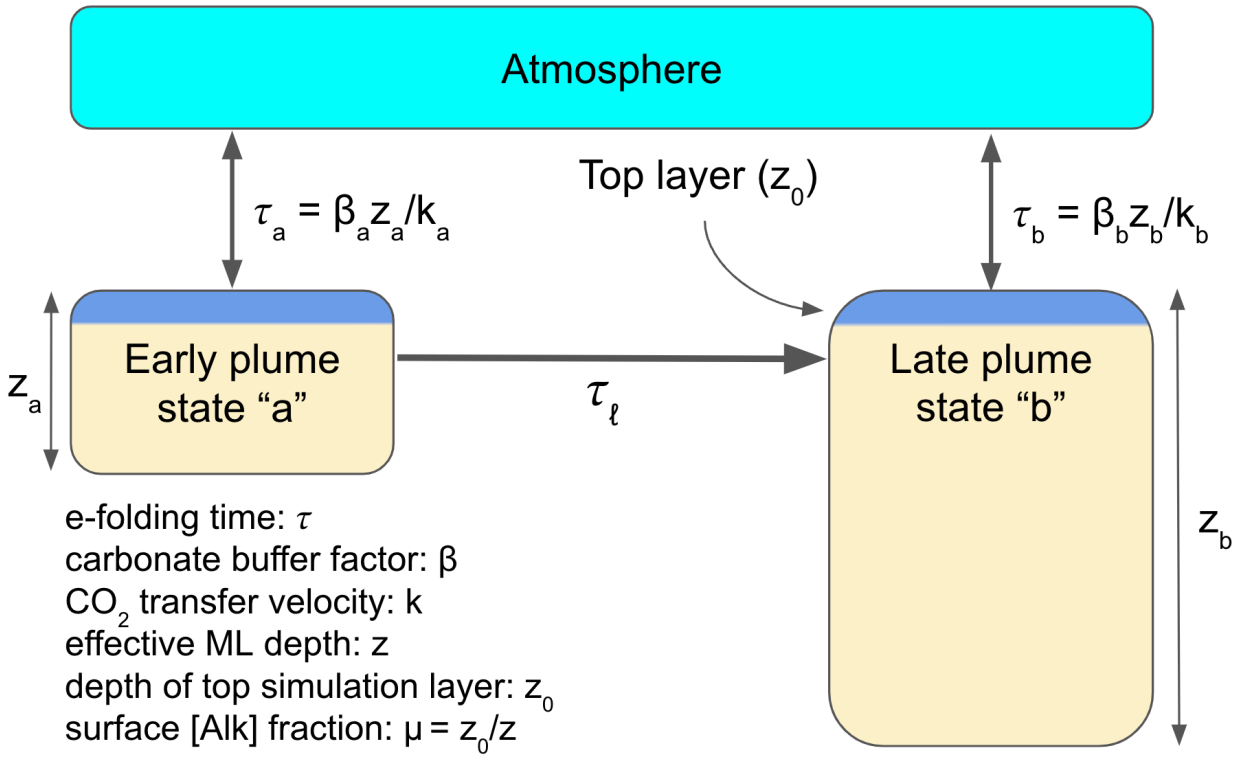

436

437 Figure 3. Schematic diagram of a 3-box model of CO_2 equilibration dynamics and surface
438 alkalinity dilution, following alkalinity addition. pCO_2 is assumed to be constant in the
439 atmosphere. We model the time evolution of an alkalinity plume as a mass flow from an early
440 plume state "a" and late plume state "b", which follows a simple diffusion law governed by the
441 e-folding time τ_ℓ. During the mass transfer, we assume that equilibration of the deficit occurs
442 from both states according to the respective e-folding times τ_a and τ_b. In general, we expect τ_a
443 << τ_b, since the surface dilution in reservoir "b" is greater due to its greater depth. In each
444 plume state, the e-folding time τ is determined by a gas exchange velocity k, an effective
445 mixed-layer depth z and a carbonate buffer factor β. The effective mixed-layer depth z is
446 determined by the depth of the top-most simulation layer z_0 and the surface dilution factor μ.
447 These equilibration parameters change from the early plume state "a" to the later plume state
448 "b".

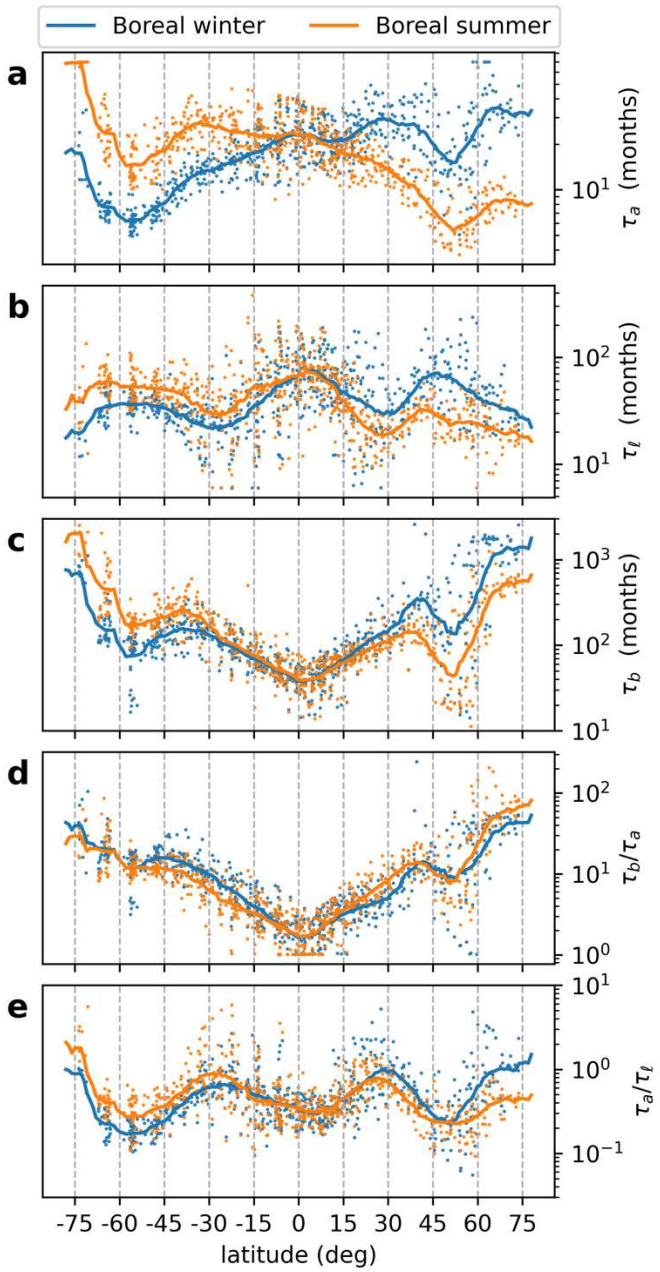

449

450 Figure 4. Fitted parameters plotted against latitude for January and July pulse releases. Each
451 point represents a single injection and subsequent uptake curve. A moving geometric average is
452 plotted (moving window of ±4°). (a) τ_a, the early e-folding time; (b) τ_ℓ, the timescale of
453 transition from "a" to "b"; (c) τ_b, the late e-folding time; (d) the ratio τ_b/τ_a, which quantifies
454 the degree of slowdown over the timescale τ_ℓ. (e) the ratio τ_a/τ_ℓ, which quantifies how much
455 equilibration will occur from initial plume state "a".

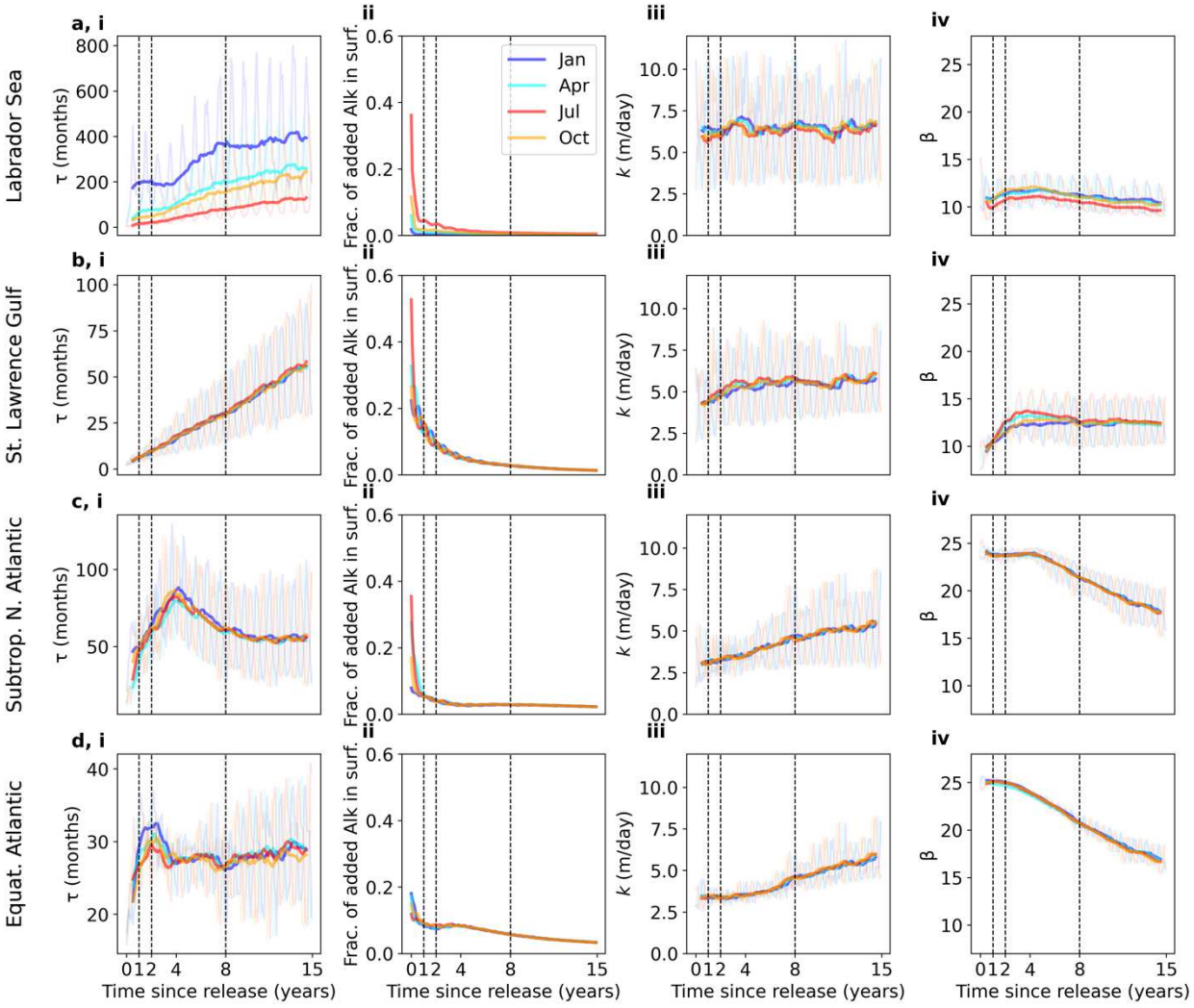

456

457 Figure 5. Four representative locations as in Figure 2, with (i) air-sea CO_2 equilibration timescale
458 τ, (ii) fraction of added alkalinity remained in the surface layer (top 10 m), (iii) gas transfer
459 velocity (k), and (iv) β. τ, k, and β were weighted by the surface CO_2 flux at each time step as
460 the plume of added alkalinity spreads out. Solid lines in (i), (iii), and (iv) are 12 months rolling
461 mean of the corresponding faded curves for the four seasons.

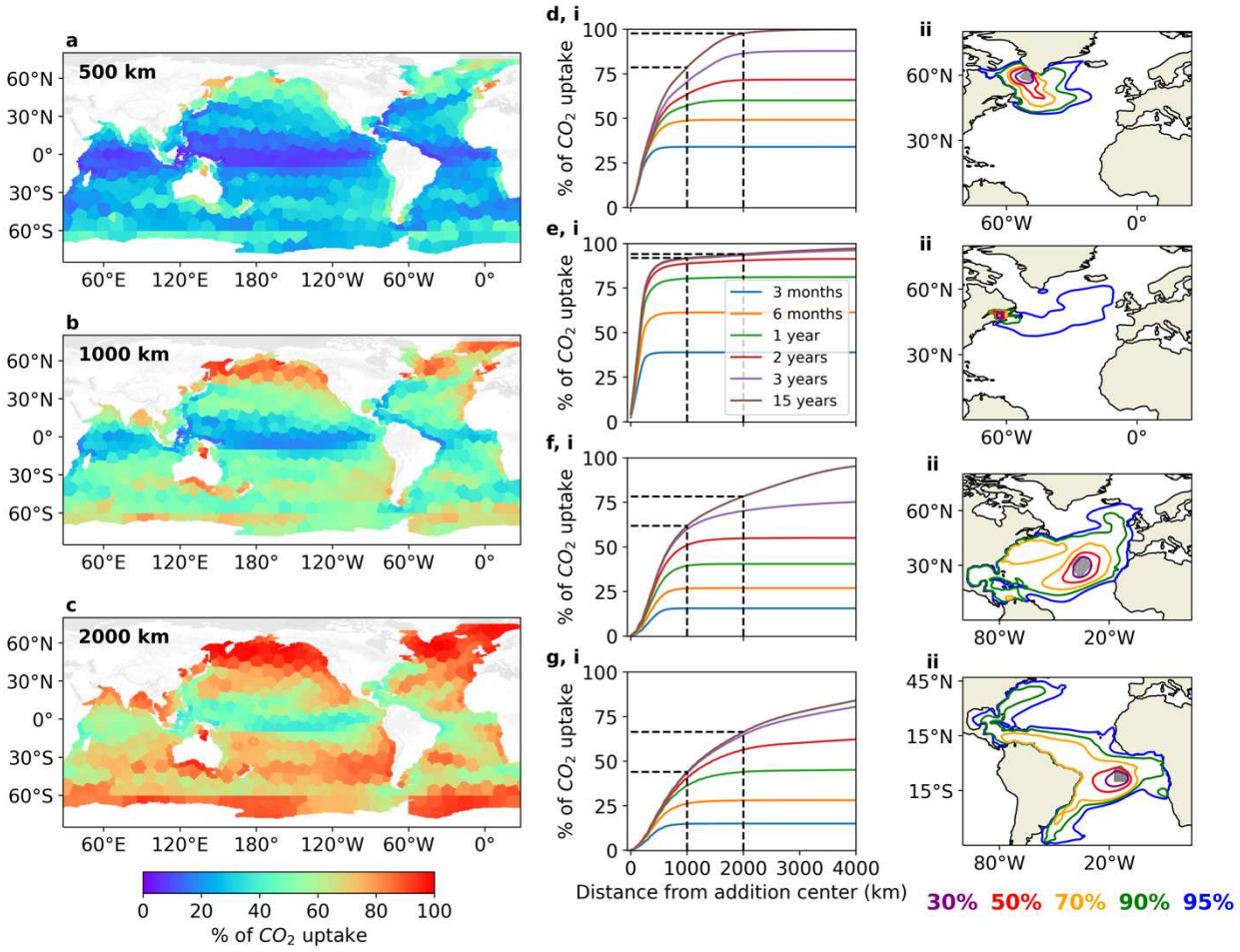

462

463 Figure 6. Percentage of cumulative CO_2 uptake after 15 years following alkalinity addition
464 occurred within (a) 500 km, (b) 1000 km, and (c) 2000 km of the alkalinity addition centers. The
465 values displayed in the global maps represent averages over experiments conducted in four
466 seasons in each polygon. (d-g) are the same 4 representative locations as in Figure 2 & 5, with
467 (i) cumulative percentages of CO_2 uptake plotted against the distance from the center of
468 alkalinity injection after 3, 6 months, 1, 3, and 15 years following alkalinity additions; (ii) spatial
469 distribution of CO_2 uptake at year 15, with each contour line enclosing the minimum area for
470 integration to reach a specific percentage of CO_2 uptake. Percentages in this figure were
471 calculated with respect to the total CO_2 uptake at year 15.

References for

"Mapping the global variation in the efficiency of ocean alkalinity enhancement for carbon dioxide removal"

1. Calvin, K. *et al. IPCC, 2023: Climate Change 2023: Synthesis Report. Contribution of Working Groups I, II and III to the Sixth Assessment Report of the Intergovernmental Panel on Climate Change [Core Writing Team, H. Lee and J. Romero (eds.)]. IPCC, Geneva, Switzerland.* https://www.ipcc.ch/report/ar6/syr/ (2023) doi:10.59327/IPCC/AR6-9789291691647.
2. Summary for Policymakers. in *Climate Change 2021 – The Physical Science Basis* 3–32 (Cambridge University Press, 2023). doi:10.1017/9781009157896.001.
3. Wang, H. *et al.* Simulated Impact of Ocean Alkalinity Enhancement on Atmospheric CO2 Removal in the Bering Sea. *Earth's Futur.* 11, (2023).
4. *Guide to Best Practices in Ocean Alkalinity Enhancement Research*. https://sp.copernicus.org/articles/2-oae2023/ (2023) doi:10.5194/sp-2-oae2023,2023.
5. Berner, R. A., Lasaga, A. C. & Garrels, R. M. The carbonate-silicate geochemical cycle and its effect on atmospheric carbon dioxide over the past 100 million years. *Am. J. Sci.* 283, 641–683 (1983).
6. Kheshgi, H. S. Sequestering atmospheric carbon dioxide by increasing ocean alkalinity. *Energy* 20, 915–922 (1995).
7. Zeebe, E. Richard, Wolf-Gladrow, D. CO2 in seawater: Equilibrium, Kinetics, Isotopes. *Elsevier* (2001).
8. Renforth, P. & Henderson, G. Assessing ocean alkalinity for carbon sequestration. *Rev. Geophys.* 55, 636–674 (2017).
9. Jones, D. C., Ito, T., Takano, Y. & Hsu, W. Spatial and seasonal variability of the air-sea equilibration timescale of carbon dioxide. *Global Biogeochem. Cycles* 28, 1163–1178 (2014).
10. He, J. & Tyka, M. D. Limits and CO2 equilibration of near-coast alkalinity enhancement. *Biogeosciences* 20, 27–43 (2023).
11. Burt, D. J., Fröb, F. & Ilyina, T. The Sensitivity of the Marine Carbonate System to Regional

Ocean Alkalinity Enhancement. *Front. Clim.* 3, (2021).

12. Tyka, M. D., Van Arsdale, C. & Platt, J. C. CO2 capture by pumping surface acidity to the deep ocean. *Energy Environ. Sci.* 15, 786–798 (2022).
13. Köhler, P., Abrams, J. F., Völker, C., Hauck, J. & Wolf-Gladrow, D. A. Geoengineering impact of open ocean dissolution of olivine on atmospheric CO2 , surface ocean pH and marine biology. *Environ. Res. Lett.* 8, 014009 (2013).
14. González, M. F. & Ilyina, T. Impacts of artificial ocean alkalinization on the carbon cycle and climate in Earth system simulations. *Geophys. Res. Lett.* 43, 6493–6502 (2016).
15. Feng, E. Y., Koeve, W., Keller, D. P. & Oschlies, A. Model-Based Assessment of the CO2 Sequestration Potential of Coastal Ocean Alkalinization. *Earth's Futur.* 5, 1252–1266 (2017).
16. Ilyina, T., Wolf-Gladrow, D., Munhoven, G. & Heinze, C. Assessing the potential of calcium-based artificial ocean alkalinization to mitigate rising atmospheric CO2 and ocean acidification. *Geophys. Res. Lett.* 40, 5909–5914 (2013).
17. Keller, D. P., Feng, E. Y. & Oschlies, A. Potential climate engineering effectiveness and side effects during a high carbon dioxide-emission scenario. *Nat. Commun.* 5, 3304 (2014).
18. Kwiatkowski, L., Berger, M., Bopp, L., Doléac, S. & Ho, D. T. Contrasting carbon dioxide removal potential and nutrient feedbacks of simulated ocean alkalinity enhancement and macroalgae afforestation. *Environ. Res. Lett.* 18, 124036 (2023).
19. Tamsitt, V. *et al.* Spiraling pathways of global deep waters to the surface of the Southern Ocean. *Nat. Commun.* 8, 172 (2017).
20. Ho, D. T. *et al.* Measurements of air-sea gas exchange at high wind speeds in the Southern Ocean: Implications for global parameterizations. *Geophys. Res. Lett.* 33, (2006).
21. Wanninkhof, R. Relationship between wind speed and gas exchange over the ocean revisited. *Limnol. Oceanogr. Methods* 12, 351–362 (2014).
22. Long, M. C. *et al.* Simulations With the Marine Biogeochemistry Library (MARBL). *J. Adv. Model. Earth Syst.* 13, (2021).

23. Bach, L. T. The additionality problem of ocean alkalinity enhancement. *Biogeosciences* 21, 261–277 (2024).
24. Danabasoglu, G. *et al.* The Community Earth System Model Version 2 (CESM2). *J. Adv. Model. Earth Syst.* 12, (2020).
25. Yeager, S. G. *et al.* The Seasonal-to-Multiyear Large Ensemble (SMYLE) prediction system using the Community Earth System Model version 2. *Geosci. Model Dev.* 15, 6451–6493 (2022).
26. Kobayashi, S. *et al.* The JRA-55 Reanalysis: General Specifications and Basic Characteristics. *J. Meteorol. Soc. Japan. Ser. II* 93, 5–48 (2015).
27. Oschlies, A. Impact of atmospheric and terrestrial CO2 feedbacks on fertilization-induced marine carbon uptake. *Biogeosciences* 6, 1603–1613 (2009).
28. Friedlingstein, P. *et al.* Global Carbon Budget 2023. *Earth Syst. Sci. Data* 15, 5301–5369 (2023).

Supplementary Files

This is a list of supplementary files associated with this preprint. Click to download.

- ZhouTykaetalSupplementary.pdf
- SupplementaryAnimationGulfStLawrence632seasons.mp4
- SupplementaryAnimationSubtropicalAtlantic1422seasons.mp4
- SupplementaryAnimationGreenland02seasons.mp4
- SupplementaryAnimationEquatorialAtlantic1292seasons.mp4